



**HAL**  
open science

# Patterning of the Surface Electrical Potential on Chalcogenide Glasses by a Thermoelectrical Imprinting Process

Ricardo Alvarado, Lara Karam, Redouane Dahmani, Antoine Lopicard, Florian Calzavara, Andréa Piarristeguy, Annie Pradel, Thierry Cardinal, Frédéric Adamietz, Evelyne Fargin, et al.

► **To cite this version:**

Ricardo Alvarado, Lara Karam, Redouane Dahmani, Antoine Lopicard, Florian Calzavara, et al.. Patterning of the Surface Electrical Potential on Chalcogenide Glasses by a Thermoelectrical Imprinting Process. *Journal of Physical Chemistry C*, 2020, 124 (42), pp.23150-23157. 10.1021/acs.jpcc.0c06507. hal-02977422

**HAL Id: hal-02977422**

**<https://hal.science/hal-02977422>**

Submitted on 10 Aug 2021

**HAL** is a multi-disciplinary open access archive for the deposit and dissemination of scientific research documents, whether they are published or not. The documents may come from teaching and research institutions in France or abroad, or from public or private research centers.

L'archive ouverte pluridisciplinaire **HAL**, est destinée au dépôt et à la diffusion de documents scientifiques de niveau recherche, publiés ou non, émanant des établissements d'enseignement et de recherche français ou étrangers, des laboratoires publics ou privés.

1  
2  
3  
4  
5  
6  
7 Patterning of the surface electrical potential on  
8  
9  
10  
11 chalcogenide glasses by a thermo-electrical  
12  
13  
14  
15 imprinting process  
16  
17  
18  
19

20 *Ricardo Alvarado*<sup>a, ‡</sup>, *Lara Karam*<sup>a, ‡</sup>, *Redouane Dahmani*<sup>a</sup>, *Antoine Lopicard*<sup>a</sup>, *Florian*  
21 *Calzavara*<sup>b</sup>, *Andréa Piarristeguy*<sup>c</sup>, *Annie Pradel*<sup>c</sup>, *Thierry Cardinal*<sup>b</sup>, *Frédéric Adamietz*<sup>a</sup>,  
22 *Evelyne Fargin*<sup>b</sup>, *Matthieu Chazot*<sup>a, d</sup>, *Kathleen Richardson*<sup>d</sup>, *Luc Vellutini*<sup>a</sup>, *Marc Dussauze*<sup>a\*</sup>  
23  
24  
25  
26  
27

28 <sup>a</sup> Institut des Sciences Moléculaires, UMR 5255, Université de Bordeaux, 351 cours de  
29  
30  
31  
32 la Libération, Talence Cedex 33405, France  
33  
34

35 <sup>b</sup> Institut de Chimie de la Matière Condensée de Bordeaux, Université de Bordeaux, 87  
36  
37  
38  
39 Avenue du Dr Schweitzer, Pessac F-33608, France  
40  
41

42 <sup>c</sup> Institut Charles Gerhardt Montpellier, UMR 5253 CNRS-UM-ENSCM, Université de  
43  
44  
45  
46 Montpellier, Place E. Bataillon, Bât 15, cc 1503, 34095 Montpellier cedex 5 – France  
47  
48

49 <sup>d</sup> Department of Materials Science and Engineering, College of Optics and Photonics,  
50  
51  
52  
53 University of Central Florida, Orlando, FL, United States  
54  
55  
56  
57  
58  
59  
60

1  
2  
3 KEYWORDS:  
45 Surface potential, Chalcogenide glasses, poling, glass structure  
6  
7  
8  
9  
10  
11  
12  
13  
14  
1516 ABSTRACT  
17  
18  
1920 The development of novel sensing systems requires breakthroughs in the conception of  
21 multifunctional materials. In this sense, while extensive research has been dedicated to the  
22 individual tuning of the electrical or optical properties of different materials, the combination of  
23 both features would result in a promising field of research that would further extend opportunities  
24 for engineering novel function in sensor geometries. In the present work, we employed a highly  
25 attractive optical material for mid-infrared (MIR) sensing (chalcogenide glasses, ChG) and  
26 focused on the spatial control of its surface electrical potential via a thermoelectrical imprinting  
27 process. Different glass compositions based on the system Ge-Sb-S-Na were prepared by varying  
28 the sulfur stoichiometry and the sodium content. Each glass was thermally poled using electrodes  
29 with specific patterns, and subsequent structural modifications and surface electrical potential were  
30 then evaluated via Raman spectroscopy and Kelvin Probe Force Microscopy (KPFM). Raman  
31 cartographies show structural modifications attributed to alkali depletion following the patterns of  
32 the electrodes used for the imprinting process. Furthermore, KPFM measurements show clearly  
33 defined motifs on the electrical potential which are associated to charges implanted into the glass  
34 matrix. It was shown that the surface potential can vary in sign within an amplitude range of 10V  
35 and exhibit patterning at the micrometer scale. We observed that the efficiency of the surface  
36  
37  
38  
39  
40  
41  
42  
43  
44  
45  
46  
47  
48  
49  
50  
51  
52  
53  
54  
55  
56  
57  
58  
59  
60

1  
2  
3 potential imprinted was dramatically impacted by the glass' sulfur and sodium content. Our results  
4  
5 demonstrate for the first time the use of a one-step process, thermal poling, for large scale  
6  
7 patterning of the surface potential of ChG creating a multi-functional material.  
8  
9

## 10 11 12 Introduction

13  
14  
15 In the context of lab-on-chip and other nanotechnological systems, control of a  
16  
17 material's electrical functionality is a valuable lever that, if tunable, offers design flexibility  
18  
19 to enhance device performance. The patterning of the electrical potential on the surface  
20  
21 at micrometer or nanometer scale has been proven to be an effective strategy to  
22  
23 assemble nanoparticles or nano-objects precisely at a desired location on a substrate  
24  
25 through electrophoresis<sup>1</sup>. Xerography is a well-recognized technique that uses  
26  
27 electrostatic forces to allow selective attachment of toner particles<sup>2</sup>. Since its early  
28  
29 development, the technique has evolved considerably such that one can now talk about  
30  
31 micro<sup>3</sup> or even nanoxerography<sup>4-6</sup>. The electrical patterning of the substrate, an  
32  
33 appropriate charge carrier or electret, can be realized through atomic force  
34  
35 microscopy<sup>1,4,6</sup>, electron beam<sup>7</sup> or focused ion beam<sup>8</sup> with a lateral resolution of about a  
36  
37 hundred nanometers. The main limitation of these techniques is that they are time  
38  
39  
40  
41  
42  
43  
44  
45  
46  
47  
48  
49  
50  
51  
52  
53  
54  
55  
56  
57  
58  
59  
60

1  
2  
3 consuming when large areas (centimeter square) are considered. To circumvent this  
4  
5  
6  
7 problem parallel printing processes to pattern charges on the electret over sizes  
8  
9  
10 approaching a centimeter square, during a single process cycle have been  
11  
12  
13 developed<sup>3,5,9,10</sup>. This stamp-like process doesn't deteriorate the resolution and even  
14  
15  
16 lower resolution (to 50 nm) can be obtained when a localized fringing field<sup>10</sup> is induced to  
17  
18  
19 direct the nanoparticle assembly. Guiding the growth of nano-objects on specific sites is  
20  
21  
22 not the only possibility that offers surface potential patterning. Rapid and reversible  
23  
24  
25 changes induced by potential to alter the focal length of liquid lenses has been achieved  
26  
27  
28 by tuning the electrochemical desorption of self-assembled monolayers (SAMs) onto a  
29  
30  
31 metal surface<sup>11</sup>. It is also possible to induce dynamic changes in interfacial properties  
32  
33  
34 such as wettability by generating conformational transitions of single layered amphiphilic  
35  
36  
37 molecules deposited onto a metallic substrate: a change in the sign of the potential leads  
38  
39  
40 to a transition between hydrophilic (molecules are straight) and hydrophobic (molecules  
41  
42  
43 are bent) nature of the surface<sup>12</sup>.  
44  
45  
46  
47  
48  
49  
50  
51

52 Research efforts towards the development of components merging multiple  
53  
54  
55 functionalities are more and more essential. In this context, the combination of electrical  
56  
57  
58  
59  
60

1  
2  
3 and optical functionalities on a single material represents a great benefit. Optical glasses  
4  
5  
6  
7 such as chalcogenides (ChG) are particularly interesting for sensing applications, as they  
8  
9  
10 are transparent in the MIR, the spectral region in which the organic molecules fingerprint  
11  
12  
13 can be found. In this study, we demonstrate for the first time the patterning of the surface  
14  
15  
16 electrical potential of Ge-Sb-S-Na glasses via a one-step imprinting process covering  
17  
18  
19 large areas at once (centimeter square scale): thermal poling. This process consists in  
20  
21  
22 applying a DC field to a glass heated at moderate temperature; the glass is brought back  
23  
24  
25 to ambient temperature with the DC field still on. This freezes the electrical constraint at  
26  
27  
28 the surface of the glass and induces several other modifications: depletion of cations<sup>13</sup>,  
29  
30  
31 structural rearrangements<sup>14–16</sup>, modification of the surface reactivity<sup>17–19</sup>, wettability  
32  
33  
34 change<sup>20</sup>, surface potential<sup>21</sup>, changes of the optical properties (modification of the  
35  
36  
37 index<sup>22</sup> and induced second order nonlinear response<sup>23–27</sup>) as well as the formation and  
38  
39  
40 patterning of glass-metal nanocomposites<sup>28–31</sup>. The patterning of these changes has been  
41  
42  
43 realized using structured electrodes that act like stamps to control the glass' surface  
44  
45  
46 properties leading to the design of functional elements such as linear<sup>19</sup> and nonlinear  
47  
48  
49 diffraction gratings<sup>32</sup> or arrays of micro-lenses<sup>33</sup>. In this study, we present evidence of the  
50  
51  
52  
53  
54  
55  
56  
57  
58  
59  
60

1  
2  
3 viability in patterning of surface electrical potentials in glasses at the micrometer scale.  
4  
5

6  
7 Through parallel studies illustrating the influence of the glass' sodium and sulfur content  
8  
9  
10 on these surface properties combined with Raman microscopy, we proposed a  
11  
12  
13 mechanistic explanation as to the origin of the surface potential in order to generate  
14  
15  
16  
17 effective and stable patterns for future applications.  
18  
19

## 20 **Experimental Methods**

21  
22  
23 *Synthesis of ChG glasses:* ChG glasses were prepared using high purity elemental Ge, Sb and S  
24  
25 (Alfa Aesar, 99.999%). Anhydrous sodium sulfide (purity unspecified) was used to incorporate  
26  
27 sodium as doping agent. Based on the stoichiometric composition  $\text{Ge}_{25}\text{Sb}_{10}\text{S}_{65}$ , different samples  
28  
29 were prepared by varying either the S to Ge ratio (i.e. increasing the sulfur content) or by keeping  
30  
31 the ratio between the other components constant and adding sodium. The nominal compositions  
32  
33 of the different glasses are reported in table 1 as well as the name by which they will be referred  
34  
35 to in the rest of the present work. Two series of glasses were synthesized: (i) A, B, C, D with  
36  
37 constant sodium content to evidence the influence of sulfur and (ii)  $\text{Na}_0$ ,  $\text{Na}_2$ ,  $\text{Na}_{5.5}$  with constant  
38  
39 S to Ge ratio to discuss the influence of the sodium content. Raw materials were weighed out in a  
40  
41 glove box under a nitrogen atmosphere before being inserted in a quartz ampule that was, then,  
42  
43 put under vacuum ( $10^{-2}$  mbar) and sealed using an oxygen-methane torch. A rocking furnace was  
44  
45 employed to ensure the homogeneity of the mixture. The temperature was increased at a rate of  
46  
47  
48  $1\text{ }^\circ\text{C min}^{-1}$  up to  $850\text{ }^\circ\text{C}$  and left at this value for 12 h for homogenization. After this period of  
49  
50  
51 time, the rocking of the furnace was stopped and the temperature was set to gradually decrease to  
52  
53  
54  $750\text{ }^\circ\text{C}$  (quenching temperature). The sample was then quenched in water and annealed for 6 h,  
55  
56  
57  
58  
59  
60

10 °C under its glass transition temperature ( $T_g$ ); the  $T_g$  of the different glasses ranging between 250 and 350 °C. Finally, glasses were cut and polished into ~1 mm thick disks of 1 cm of diameter.

	Sample's name	Composition (at. %)				S/Ge ratio
		Ge	Sb	S	Na	
Influence of the S/Ge or sulfur content	A	24.5	10	64.5	<b>1</b>	<b>2.6</b>
	B	22	10	67	<b>1</b>	<b>3</b>
	C	20	10	69	<b>1</b>	<b>3.4</b>
	D	17	10	72	<b>1</b>	<b>4.2</b>
Influence of the sodium content	Na <sub>0</sub>	22.5	10	67.5	<b>0</b>	<b>3</b>
	Na <sub>2</sub>	22	9.8	66.2	<b>2</b>	<b>3</b>
	Na <sub>5.5</sub>	21.3	9.4	64.8	<b>5.5</b>	<b>3</b>

Table 1: Atomic composition of the different glasses of interest and the name they are referred to.

*Vibrational spectroscopy:* Raman spectra were acquired using an XploRA PLUS (Horiba) spectrometer with a laser source at 785 nm focused on the sample via a 50x objective lens. Cartographies were acquired using a 100x (N.A. 0.9) objective lens on an area of 80 x 60  $\mu\text{m}$  with a lateral resolution of ~2  $\mu\text{m}$ .

*Thermoelectrical imprinting:* Electrical patterning was performed under a nitrogen atmosphere by pressing the ChG glass sample between two electrodes: a structured electrode used as a stamp located at the anode, and a silicon electrode at the cathode. A coverslip was used as a sacrificial layer in between the glass sample and the cathode. The structured electrode consists of a 100 nm thick Ti-Pt metallic films deposited on a silicate glass slide. The patterned electrode was prepared by a classical lithography process resulting in squared motifs (40x40 or 30x30  $\mu\text{m}$ ) leaving a 4  $\mu\text{m}$  width electrically conductive Pt grid. The system was then heated to 210 °C, after reaching thermal stabilization, an electric field was applied at 375  $\text{V}\cdot\text{min}^{-1}$  up to 0.9 kV. The temperature and DC

1  
2  
3 bias were kept constant for 30 min, then, the system was cooled down to room temperature before  
4  
5 removal of the electric field.  
6

7  
8 *Characterization of surface electrical potential:* Measurements were performed at 100 nm from  
9  
10 the surface by an AFM Dimensions Icon (Bruker) on PeakForce KPFM mode using a PFQNE-AL  
11  
12 cantilever, over a 55 x 55  $\mu\text{m}$  area and a resolution of 1024 points per line.  
13

## 14 **Results**

### 15 *Structural analysis of pristine glasses*

16  
17 Raman spectra of each pristine sample were acquired and normalized over their total integrated  
18  
19 area (**Figure 1**). Different models to describe  $\text{GeS}_2$  glass networks have been proposed in the  
20  
21 literature<sup>34–37</sup> resulting in different assignments for the characteristic Raman bands associated with  
22  
23 this network.<sup>38–40</sup> A recent article regarding multimodal structural characterization of Ge-S-I<sup>39</sup> as  
24  
25 well as previously reported DFT calculations<sup>40</sup> were used for the assignments in this work. The  
26  
27 spectra presented in **Figure 1a** show different contributions associated with the stretching modes  
28  
29 of Ge-S bonds in corner sharing (CS)  $\text{GeS}_4$  tetrahedra<sup>39,40</sup> around  $340\text{ cm}^{-1}$  and  $415\text{ cm}^{-1}$  as well  
30  
31 as Sb-S stretching modes in  $\text{SbS}_3$  pyramids<sup>41</sup> resulting in a small shoulder around  $300\text{ cm}^{-1}$ . The  
32  
33 most striking variation when the amount of sulfur increases (i.e. going from glass A to D) is the  
34  
35 apparition of new bands at  $152\text{ cm}^{-1}$ ,  $219\text{ cm}^{-1}$  and  $474\text{ cm}^{-1}$ , they correspond to S-S bonds.<sup>39,42,43</sup>  
36  
37 The first two bands, present only when the sulfur content exceeds 70 at.%, are linked to the  
38  
39 formation of sulfur rings ( $\text{S}_8$ ) inside the glass matrix.<sup>39,42</sup> Another evolution when increasing the  
40  
41 sulfur content, is the regular decrease of the contribution of the Ge related entities ( $340$  and  $415\text{ cm}^{-1}$ ).  
42  
43 This is consistent with the decrease of the Ge content in the composition when going from  
44  
45 composition A to D. The Raman intensity of the modes related to Sb are not affected which is  
46  
47 consistent with the fact the Sb content stays constant. More interestingly, the modes related to  
48  
49  
50  
51  
52  
53  
54  
55  
56  
57  
58  
59  
60

1  
2  
3 either the Ge or Sb entities are observed at the same wavenumber, no frequency shift can be  
4  
5 observed when the sulfur content increases. These observations suggest that the surplus of sulfur  
6  
7 does not alter the glass forming units but rather the interconnections among them by establishing  
8  
9 new homopolar S-S linkages. This results in the creation of S-S chains up to a given sulfur content  
10  
11 (close to 70 at.%), passed this value, the increase of the sulfur content results in its organization  
12  
13 into rings not linked to the other glass entities.  
14  
15  
16  
17

18 Let us focus on the effect of the sodium addition to the glass network (with fixed S to Ge ratio)  
19  
20 on the basis of the Raman spectra presented in **Figure 1b**. Looking at the Raman response of  
21  
22 samples  $\text{Na}_0$  to  $\text{Na}_{5.5}$ , it appears that only slight changes can be observed when the sodium content  
23  
24 varies from 0 to 5.5 at.%. In order to highlight these spectral variations, the difference Raman  
25  
26 spectrum is presented in **Figure 1c**. It corresponds to the Raman spectrum of a sodium rich glass  
27  
28 ( $\text{Na}_{5.5}$ ) subtracted to the one of the glass without sodium ( $\text{Na}_0$ ). Multiple contributions from  $\text{GeS}_4$   
29  
30 tetrahedra can be observed ( $333, 375, 408$  and  $445 \text{ cm}^{-1}$ )<sup>40</sup>. The peaks at  $\sim 333 \text{ cm}^{-1}$  and  $\sim 408 \text{ cm}^{-1}$   
31  
32 can be ascribed to CS conformation<sup>40</sup> while the valleys at  $\sim 375 \text{ cm}^{-1}$  and  $\sim 445 \text{ cm}^{-1}$  are  
33  
34 representative to an Edge Sharing (ES) arrangement<sup>40</sup>. The bands corresponding to the CS  
35  
36 tetrahedra appear positive in the Raman difference spectra ( $\text{Na}_0$  minus  $\text{Na}_{5.5}$ ) while those related to  
37  
38 the ES are negative. This evolution denotes a modification of the interconnections of the germanate  
39  
40 network with the addition of sodium as part of the CS tetrahedral units are substituted for the ES  
41  
42 tetrahedra conformation. A peak at  $304 \text{ cm}^{-1}$  and a valley at around  $264 \text{ cm}^{-1}$  are present in the  
43  
44 difference spectra and can be attributed to the contribution of antimony glass forming units. The  
45  
46 addition of sodium in the vicinity of a  $\text{SbS}_3$  pyramidal units can affect the strength of the Sb-S  
47  
48 bonds. Therefore, the lower frequency of the band at  $264 \text{ cm}^{-1}$  for the sodium rich glasses ( $\text{Na}_{5.5}$ )  
49  
50  
51  
52  
53  
54  
55  
56  
57  
58  
59  
60

as compared to  $304\text{ cm}^{-1}$  without sodium ( $\text{Na}_0$ ) could be linked to weaker Sb-S bonds as part of the unit electronegativity is now distributed within the sodium coordination shell.

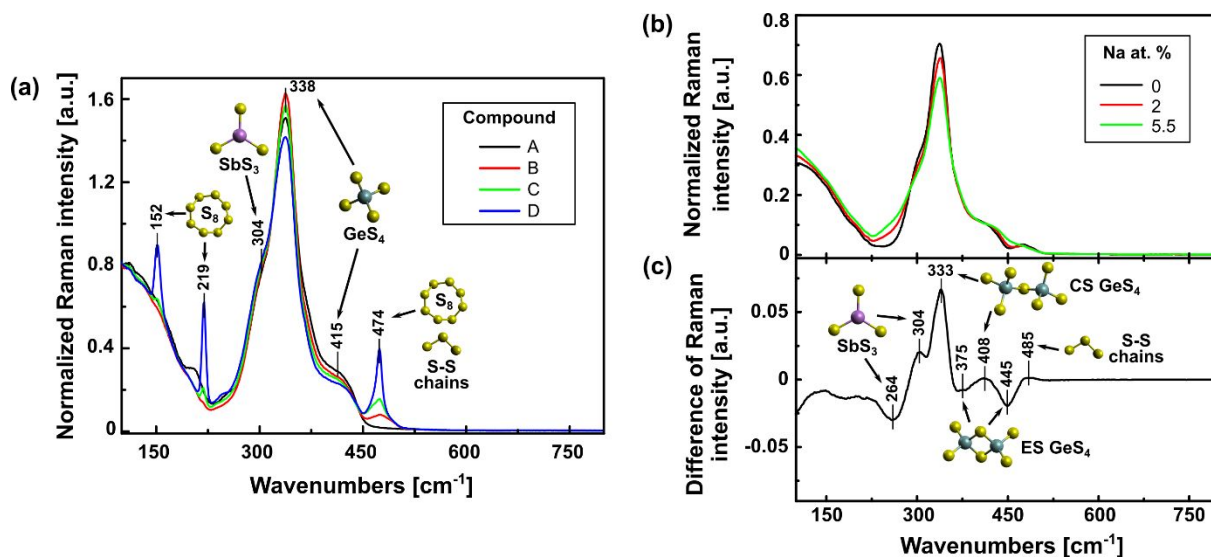


**Figure 1.** Raman spectra of the pristine ChG samples: (a) A, B, C and D glasses series with increasing S/Ge ratio, (b)  $\text{Na}_0$ ,  $\text{Na}_2$  and  $\text{Na}_{5.5}$  glasses series with increasing sodium content and constant ratio between the other components and (c) Raman difference spectra: response of  $\text{Na}_{5.5}$  subtracted to  $\text{Na}_0$  response.

### *Spatial distribution of sodium after thermoelectrical imprinting*

The thermally poled glasses were studied by Raman spectroscopy to evidence the structural variations induced by the process. Based on previous studies,<sup>32,33</sup> a spatial control of the sodium concentration through the use of a structured electrode is expected on the post-poling surface. In **Figure 2a**, are presented the Raman spectra from the post-poling surface of the A composition. The spectra were extracted from the regions that were *in contact* (IC) with the Ti-Pt metallic areas and *not in contact* (NC) with these conductive zones (i.e. middle of the squared patterns of the electrode). The variations between the two spectra are weak, thus, in order to highlight them, the Raman difference spectrum is presented **Figure 2b**. It corresponds to the spectrum extracted from

1  
2  
3 the NC region subtracted to the IC region. The resulting Raman difference spectrum closely  
4 matches the one presented in **Figure 1c** ( $\text{Na}_0$  minus  $\text{Na}_{5.5}$ ). Such similarity suggests in the IC zone  
5 the structure approaches the structure of a glass without sodium. This confirms the sodium  
6 depletion under the conductive zones of the electrode previously reported.<sup>26</sup> A similar  
7 methodology has been applied to the glasses presenting different S/Ge ratio (with same initial  
8 sodium content). The resulting spectra and Raman difference spectra are presented **Figure 3**. The  
9 ones of glass A have been reproduced for comparison with two different sulfur contents (glass  
10 samples B and D). All the Raman difference spectra show the same evolution. For all S to Ge ratio,  
11 thermal poling has the same effect: the post-poling glass in the IC zone shows a structure similar  
12 to a pristine glass without sodium. This shows the flexibility of the glass matrix which is rearranged  
13 through poling whatever the initial composition. **Figure 2c** are presented the Raman cartographies  
14 associated with selected bands of the Raman difference spectrum showing the spatial distribution  
15 of the structural rearrangements. The same pattern is observed for the distribution of all bands  
16 demonstrating the spatial coherence of the spectral variations. Furthermore, the pattern of the  
17 electrode can be recognized in these cartographies confirming that, through the use of a structured  
18 electrode, thermal poling can be successfully employed as an imprinting process. One should also  
19 notice that the imprinted patterns do not correspond exactly to the electrode design. This is due to  
20 a gradient in sodium concentration from the edge of the electrode toward the center of the non-  
21 conductive square. Such effect was accurately described in a study linked to the formation of  
22 gradient of refractive indices (GRIN) in similar glasses.<sup>26</sup>  
23  
24  
25  
26  
27  
28  
29  
30  
31  
32  
33  
34  
35  
36  
37  
38  
39  
40  
41  
42  
43  
44  
45  
46  
47  
48  
49  
50  
51  
52  
53  
54  
55  
56  
57  
58  
59  
60

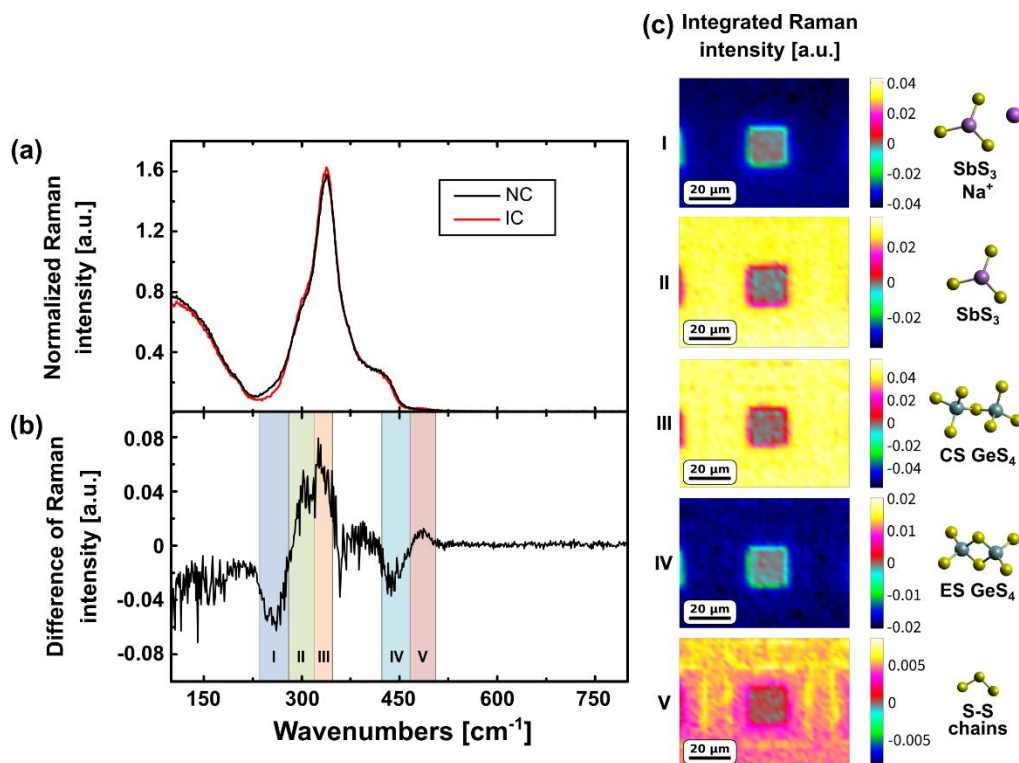


**Figure 2.** (a) Raman spectra from the thermally poled A glass, the black line corresponds to the region non in contact (NC) with the conductive zone and the red line in contact (IC). (b) Raman difference spectrum where the spectrum of the NC region has been subtracted to the IC region. (c) Spatial evolution of the Raman intensity of the different bands revealed by the Raman difference spectrum and the schematic representation of the glass units they are associated with.

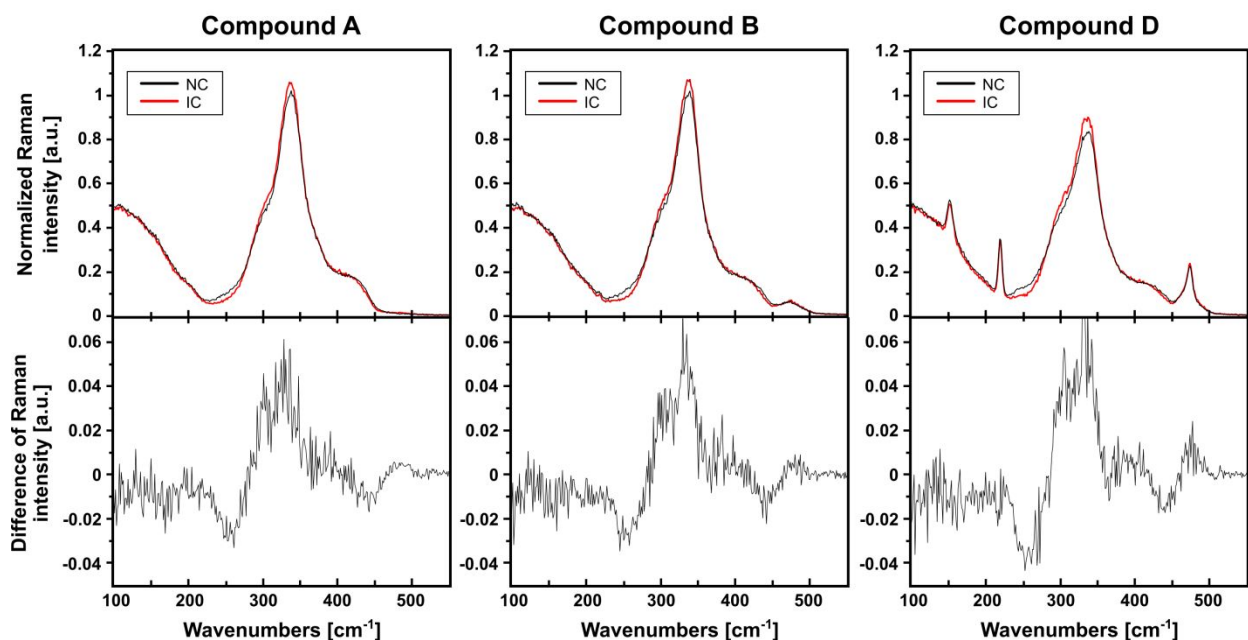


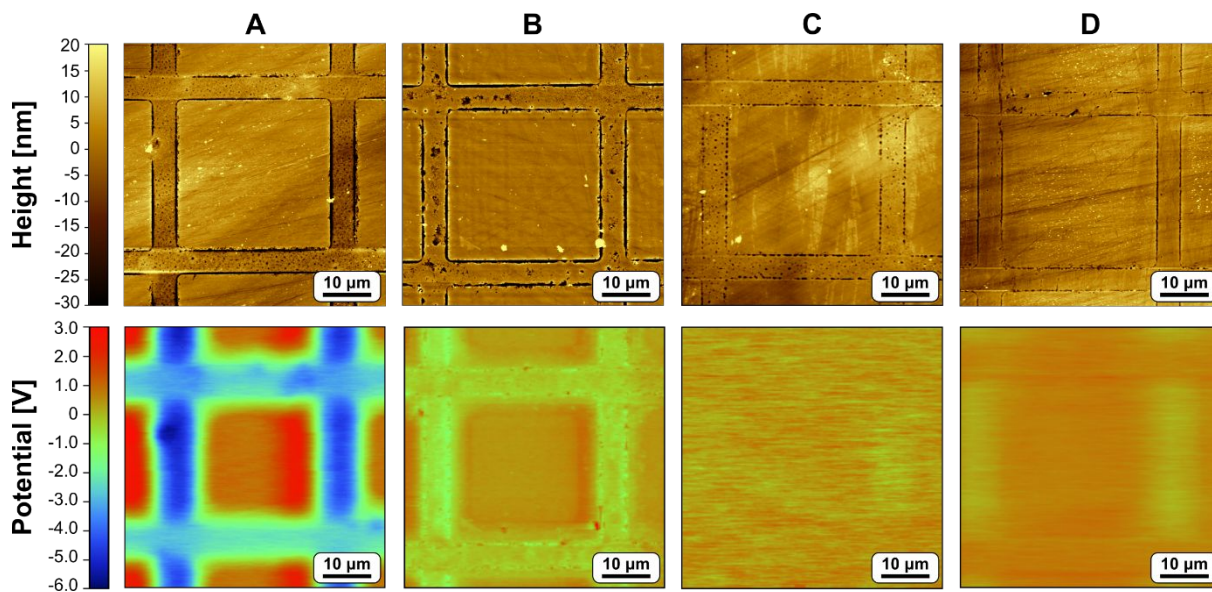
**Figure 3.** (Top) Raman spectra from the different thermally poled glasses A, B and D presenting different S/Ge ratio and same sodium content. The black lines correspond to the region not in contact (NC) with the conductive zone and the red line in contact (IC). (Bottom) Raman different spectra for each glass where the spectrum of the NC region has been subtracted from the spectrum of the IC region.

### *Patterning of the surface electrical potential*

The post-poling topography as well as the resulting surface potential magnitude and spatial distribution for all the studied glasses are presented **Figure 4** and **Figure 5**. The **Figure 4** is dedicated to the influence of the sulfur content with the series of glasses A, B, C and D (1 at. % of sodium) while in **Figure 5** the emphasis is put on the sodium content with the Na<sub>0</sub>, Na<sub>2</sub> and Na<sub>5.5</sub> glasses.

Let us focus first on the **Figure 4** with the A, B, C and D glasses. Topography variations of a maximum of 50 nm amplitude can be observed. The main changes are located at the edges of the

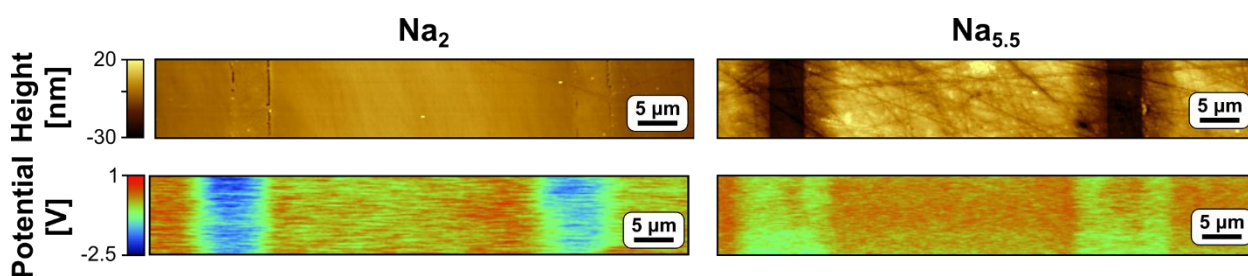
1  
2  
3 electrode; the rest of the surface is rather flat for all samples with even smaller changes as the  
4 sulfur content increases. Looking at the surface potential of the poled A glass sample, one can  
5 clearly recognize the pattern of the electrode resulting in negatively charged regions when IC with  
6 the electrode and positively charged regions when NC. The region IC, as the Raman study has  
7 shown, corresponds to a sodium-depleted region. The amplitude variation of surface potential is  
8 9 V for this sample. Glass B only shows an amplitude variation of 1 V and ~0.2-0.4 V for C and  
9 D. Based on this observation the bigger the ratio S to Ge is (i.e. the more sulfur in the matrix), the  
10 lower the magnitude of the potential is: it is maximal for glass A (stoichiometric composition) and  
11 diminishes in B until the pattern can barely be observed for glasses C and D.



45 **Figure 4.** AFM measured topography (top) and KPFM measured surface potential (bottom)  
46 images of the post-poling surface of glasses A, B, C and D i.e. increasing sulfur content with fixed  
47 sodium content.  
48  
49  
50

51  
52  
53 Regarding the influence of the sodium content the first comment we have to make is that when  
54 no sodium is present in the initial composition ( $\text{Na}_0$ ), the post-poling surface does not present any  
55  
56  
57  
58  
59  
60

1  
2  
3 topographic variation and no potential structuring is observed. For this reason, the measurements  
4 concerning this composition are not presented here. In Figure 5, can be found the post-poling  
5 topography and surface potential of glasses with higher sodium contents ( $\text{Na}_2$  and  $\text{Na}_{5.5}$ ). It appears  
6 that, for the imprinting process to be successful, the presence of alkali in the initial composition is  
7 necessary. Increasing the initial sodium content results in variation of the topography, the more  
8 the initial sodium content increases the stronger the topography changes are. The surface potential  
9 structuring can be observed for  $\text{Na}_2$  but with higher sodium contents ( $\text{Na}_{5.5}$ ), it tends to disappear.



19  
20  
21  
22  
23  
24  
25  
26  
27  
28 **Figure 5.** AFM measured topography (top) and KPFM measured surface potential (bottom)  
29 images of the post-poling surface of glasses  $\text{Na}_2$  and  $\text{Na}_{5.5}$  i.e. increasing sodium content with other  
30 component's ratios constant. The results obtained for  $\text{Na}_0$  (no sodium) are not presented as no  
31 effect – topology or potential – were observed in the absence of alkali cation in the initial  
32 composition.  
33  
34  
35  
36  
37  
38  
39

## 40 41 **Discussion**

42  
43 The main objective of this study is to engineer a spatially varying and stable surface electrical  
44 potential on a glass optical materials that could open new opportunities in the development of  
45 multifunctional approach in inorganic glass science. Charge implantation has been successfully  
46 realized in chalcogenide materials since the 70's with the development of xerography processes  
47 notably on amorphous selenium.<sup>44,45</sup> These works have demonstrated the potential of chalcogenide  
48 materials to sustain electrical or plasma processes for the fabrication of charged surfaces.  
49  
50  
51  
52  
53  
54  
55  
56  
57  
58  
59  
60

1  
2  
3 Nevertheless, in our case, the multifunctional properties targeted require novel objectives in terms  
4 of long term stability and micrometric spatial control. As compared to a xerography approach, the  
5 thermo-electrical imprinting process is considerably different because of the nature of the charge  
6 carriers as it involves necessarily alkali cations. The Raman mapping reported has evidenced the  
7 ability of this thermo-electrical process to control the sodium spatial distribution within the  
8 chalcogenide glassy matrix at the micrometer scale for all the glass compositions studied. This  
9 structural study also points out the similarity observed between spectral variations from glasses  
10 prepared with and without sodium addition (Figure 1) and the ones measured when the sodium is  
11 depleted from the glass matrix under the electrical constrain (Figure 2). It shows the flexibility of  
12 the glass network and its ability to rearrange under a high electric field at temperatures below its  
13 glass transition. Regarding the objective of surface electrical potential patterning, the presented  
14 results have also demonstrated that by using this imprinting poling process, stable surface charges  
15 can only be obtained with sodium doped glasses which denotes the importance of cationic charge  
16 carriers to modify the surface electrical properties for these germanate chalcogenide glasses.  
17  
18  
19  
20  
21  
22  
23  
24  
25  
26  
27  
28  
29  
30  
31  
32  
33  
34

35 To analyze the surface potential patterned for this series of glasses, one should consider the  
36 respective effects of: (i) the location of the trapped charges which have to be promoted close to  
37 the surface in order to influence the surface potential and (ii) the energy level of the traps which  
38 will determine the stability of the induced surface potential.  
39  
40  
41  
42  
43  
44

45 Concerning charged surface stabilities, let's remind that research studies in the domains of  
46 polarized or charged materials have demonstrated the importance of a material disorder state to  
47 enable a slow discharge<sup>46-50</sup>. Depending on the trap energy distribution, charges can diffuse to  
48 reach a "sink" to be neutralized as described in a classical trapping model developed to describe  
49 electronic relaxation in amorphous semiconductors<sup>46,51</sup>. In addition, in reference to works done on  
50  
51  
52  
53  
54  
55  
56  
57  
58  
59  
60

1  
2  
3 the photosensitivity or on thermal poling of chalcogenide glasses, it was shown that structural  
4 rearrangements induced by the optical or electrical polarization treatments are very favorable for  
5 the stability of charges as the modified structure considerably increases the energy barrier of the  
6 traps<sup>52,53</sup>.  
7  
8  
9

10  
11 To summarize the results of this study: (i) we have observed that the surface potential patterning  
12 is efficient only for the composition stoichiometric in sulfur, and (ii) if the sodium content  
13 increases, the electrical potential values decrease together with an enhancement of the surface  
14 topology variations. Both findings denote the importance of the glass local structure to achieve the  
15 targeted functional properties.  
16  
17  
18

19 Concerning the effect of the sulfur content, it is not possible to conclude if the absence of surface  
20 potential observed for the rich-sulfur glasses can be linked to an implantation of trapped charges  
21 preferentially localized in the bulk or if it can be linked to a very poor stability of charges at the  
22 surface. Nevertheless, the structural study has confirmed a significant amount of S-S homopolar  
23 bonds and the presence of sulfur rings in the glassy structure, it induces a real change in the local  
24 homogeneity and polarizability of the structure which necessarily affect the distribution of trap  
25 energies and as a consequence the local transport/diffusion of charges. Under this assumption, one  
26 may expect an easier transport of the charge carriers in the poled matrix with the increase of  
27 homopolar bonds which could locally facilitate an electronic transport in the amorphous structure.  
28 In any case, it denotes the key role of the glass local molecular structure to promote stable surface  
29 charges.  
30  
31  
32  
33  
34  
35  
36  
37  
38  
39  
40  
41  
42  
43  
44  
45  
46  
47  
48

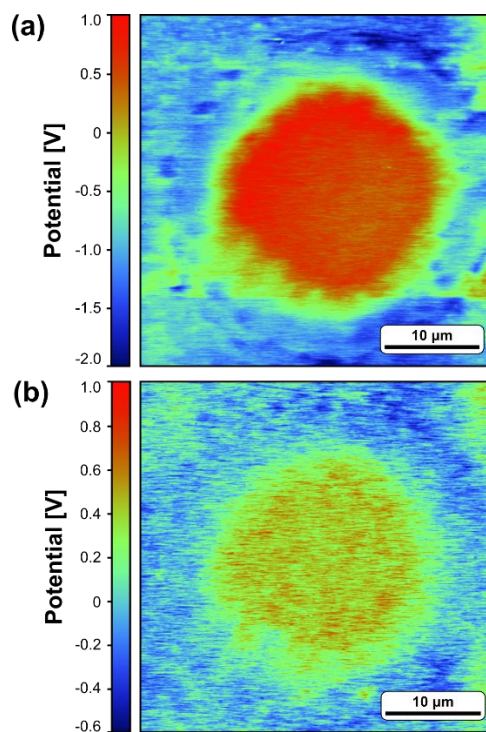
49 Focusing our analysis on the influence of the sodium content in the glass matrix, one should  
50 point out that when the amount of alkali increase the imprinting process induces non negligible  
51 surface topology variations (steps of 50 nm for 5.5 mol% of Na). This surface relief modification  
52  
53  
54  
55  
56  
57  
58  
59  
60

1  
2  
3 is expected from previous studies on poled ionic glasses<sup>54</sup>. It denotes the presence of matter  
4 displacement, volume contraction and glass density variations induced during the alkali-depleted  
5 layer formation. In such a case, we can note a clear decrease of the patterned surface potential  
6 amplitude when the amount of charge carriers involved increase imposing large modification of  
7 the physico-chemical properties of the glassy material surface.  
8  
9

10  
11  
12 Furthermore, one should evoke the spatial control of charge implantation managed by this  
13 imprinting process. In regards to a future electrical/optical multifunctional approach, a spatial  
14 control of the surface potential at the micrometer scale is essential in order to suite with the sizes  
15 of photonic waveguides for example. This study has demonstrated the potential of this polarization  
16 process to achieve such objectives. To explain the surface potential patterns obtained, one should  
17 focus on the electrode configuration. : a juxtaposition of conductive and non-conductive zones (as  
18 used in this study with a metallic thin film patterned by a lithography method). Such a juxtaposition  
19 of conductive and non-conductive area allows to promote in plane field components which can  
20 promote and control surface current direction. Such effect was recently reported for the electro-  
21 optical second harmonic generation response obtained for a similar glass system<sup>32</sup>. These surface  
22 currents controlled by the electrode geometry might be at the origin of the sign control of the  
23 surface potential which allow accurate patterning at the micrometric scale, yet further studies will  
24 be required to explain this process in detail.  
25  
26  
27  
28  
29  
30  
31  
32  
33  
34  
35  
36  
37  
38  
39  
40  
41  
42  
43

44  
45 Finally, the question of the stability of the induced patterned surface potential with time is crucial  
46 for further integration in multifunctional systems. This temporal aspect wasn't the main objective  
47 of this work, however to justify the real interest of these polarized surfaces, is presented in figure  
48 6 the surface potential measured on a sample right after the thermoelectrical treatment and 24  
49 months later. The electrode used is constituted of a circular pattern. One can observe that, if the  
50  
51  
52  
53  
54  
55  
56  
57  
58  
59  
60

1  
2  
3 amplitude variation of surface potential has significantly decreased (from 3 V to 1.6 V), the  
4 patterning of the surface potential is retained after two years. These preliminary results on the  
5  
6 patterning of the surface potential is retained after two years. These preliminary results on the  
7  
8 stability of the poled chalcogenide surface properties are encouraging. Some additional  
9  
10 characterizations are actually in progress.



36 **Figure 6.** KPFM imaging of a ChG sample after thermal poling at after being poled (a) and after  
37  
38 24 months of being poled (b).  
39

## 41 **Conclusions**

42  
43  
44  
45 A spatial control of the surface electrical potential of chalcogenide glasses in the system Ge-Sb-S-  
46  
47 Na was achieved using a thermo-electrical imprinting process. The charged chalcogenide surfaces  
48  
49 have shown electrical potentials varying in sign within an amplitude range of 10V. The induced  
50  
51 patterns can be accurate at the micrometer scale and effective on large centimeter scales.  
52  
53  
54 Combining data from structural characterization and Kelvin Probe Force Microscopy (KPFM), the  
55  
56  
57  
58  
59  
60

1  
2  
3 glass composition has been found to play a crucial role on the final electrical properties. The  
4 presence of S-S homopolar bonds and sulfur rings in glasses as well as the sodium content largely  
5 influence the induced surface potential. Such set of results open the way to create new multi-  
6 functional (optical and electrical) surfaces.  
7  
8  
9  
10  
11  
12

## 13 AUTHOR INFORMATION

### 14 15 16 **Corresponding Author**

17  
18  
19 \* E-mail: marc.dussauze@u-bordeaux.fr  
20  
21

### 22 **Author Contributions**

23  
24 The manuscript was written through contributions of all authors. All authors have given approval  
25 to the final version of the manuscript. ‡These authors contributed equally.  
26  
27  
28  
29

### 30 **Acknowledgment**

31  
32 The authors gratefully acknowledge the financial support of: IdEx Bordeaux (Cluster of  
33 Excellence LAPHIA and the allocated grant referred to as ANR-10-IDEX-03-03) and the CNRS  
34 project EMERGENCE @INC2019. This project has received funding from the European Union's  
35 Horizon 202 research program under the Marie Skłodowska-Curie grant agreement No 823941  
36 (FUNGLASS).  
37  
38  
39  
40  
41  
42  
43  
44  
45  
46

## 47 REFERENCES

- 48  
49 (1) Mesquida, P.; Stemmer, A. Attaching Silica Nanoparticles from Suspension onto  
50 Surface Charge Patterns Generated by a Conductive Atomic Force Microscope Tip.  
51 *Adv. Mater.* **2001**, *13* (18), 1395–1398. [https://doi.org/10.1002/1521-4095\(200109\)13:18<1395::AID-ADMA1395>3.0.CO;2-0](https://doi.org/10.1002/1521-4095(200109)13:18<1395::AID-ADMA1395>3.0.CO;2-0).  
52  
53  
54  
55  
56  
57  
58  
59  
60

- 1  
2  
3  
4 (2) Schaffert, R. M.; Oughton, C. D. Xerography: A New Principle of Photography and  
5 Graphic Reproduction. *J. Opt. Soc. Am.* **1948**, *38* (12), 991.  
6 <https://doi.org/10.1364/JOSA.38.000991>.
- 7  
8  
9 (3) Jacobs, H. O. Submicrometer Patterning of Charge in Thin-Film Electrets. *Science*  
10 **2001**, *291* (5509), 1763–1766. <https://doi.org/10.1126/science.1057061>.
- 11  
12 (4) Palleau, E.; Sangeetha, N. M.; Viau, G.; Marty, J.-D.; Ressier, L. Coulomb Force  
13 Directed Single and Binary Assembly of Nanoparticles from Aqueous Dispersions  
14 by AFM Nanoxerography. *ACS Nano* **2011**, *5* (5), 4228–4235.  
15 <https://doi.org/10.1021/nn2011893>.
- 16  
17 (5) Jacobs, H. O.; Campbell, S. A.; Steward, M. G. Approaching Nanoxerography: The  
18 Use of Electrostatic Forces to Position Nanoparticles with 100 Nm Scale  
19 Resolution. *Adv. Mater.* **2002**, *14* (21), 1553–1557. [https://doi.org/10.1002/1521-4095\(20021104\)14:21<1553::AID-ADMA1553>3.0.CO;2-9](https://doi.org/10.1002/1521-4095(20021104)14:21<1553::AID-ADMA1553>3.0.CO;2-9).
- 20  
21 (6) Ressier, L.; Palleau, E.; Garcia, C.; Viau, G.; Viallet, B. How to Control AFM  
22 Nanoxerography for the Templated Monolayered Assembly of 2 Nm Colloidal Gold  
23 Nanoparticles. *IEEE Trans. Nanotechnol.* **2009**, *8* (4), 487–491.  
24 <https://doi.org/10.1109/TNANO.2009.2016089>.
- 25  
26 (7) Fudouzi, H.; Kobayashi, M.; Shinya, N. Assembling 100 Nm Scale Particles by an  
27 Electrostatic Potential Field. *J. Nanoparticle Res.* **2001**, *3* (2/3), 193–200.  
28 <https://doi.org/10.1023/A:1017903123384>.
- 29  
30 (8) Fudouzi, H.; Kobayashi, M.; Shinya, N. Site-Controlled Deposition of Microsized  
31 Particles Using an Electrostatic Assembly. *Adv. Mater.* **2002**, *14* (22), 1649–1652.  
32 [https://doi.org/10.1002/1521-4095\(20021118\)14:22<1649::AID-ADMA1649>3.0.CO;2-Z](https://doi.org/10.1002/1521-4095(20021118)14:22<1649::AID-ADMA1649>3.0.CO;2-Z).
- 33  
34 (9) Ma, X.; Zhao, D.; Xue, M.; Wang, H.; Cao, T. Selective Discharge of Electrostatic  
35 Charges on Electrets Using a Patterned Hydrogel Stamp. *Angew. Chem. Int. Ed.*  
36 **2010**, *49* (32), 5537–5540. <https://doi.org/10.1002/anie.201000766>.
- 37  
38 (10) Barry, C. R.; Jacobs, H. O. Fringing Field Directed Assembly of Nanomaterials.  
39 *Nano Lett.* **2006**, *6* (12), 2790–2796. <https://doi.org/10.1021/nl0618703>.
- 40  
41 (11) Gorman, C. B.; Biebuyck, H. A.; Whitesides, G. M. Control of the Shape of Liquid  
42 Lenses on a Modified Gold Surface Using an Applied Electrical Potential across a  
43  
44  
45  
46  
47  
48  
49  
50  
51  
52  
53  
54  
55  
56  
57  
58  
59  
60

- 1  
2  
3 Self-Assembled Monolayer. *Langmuir* **1995**, *11* (6), 2242–2246.  
4 <https://doi.org/10.1021/la00006a063>.  
5  
6  
7 (12) Lahann, J. A Reversibly Switching Surface. *Science* **2003**, *299* (5605), 371–374.  
8 <https://doi.org/10.1126/science.1078933>.  
9  
10 (13) Dussauze, M.; Fargin, E.; Lahaye, M.; Rodriguez, V.; Adamietz, F. Large Second-  
11 Harmonic Generation of Thermally Poled Sodium Borophosphate Glasses. *Opt.*  
12 *Express* **2005**, *13* (11), 4064–4069.  
13  
14 (14) Dussauze, M.; Kamitsos, E. I.; Fargin, E.; Rodriguez, V. Structural Rearrangements  
15 and Second-Order Optical Response in the Space Charge Layer of Thermally  
16 Poled Sodium–Niobium Borophosphate Glasses. *J. Phys. Chem. C* **2007**, *111* (39),  
17 14560–14566. <https://doi.org/10.1021/jp074335f>.  
18  
19 (15) Dussauze, M.; Rodriguez, V.; Lipovskii, A.; Petrov, M.; Smith, C.; Richardson, K.;  
20 Cardinal, T.; Fargin, E.; Kamitsos, E. I. How Does Thermal Poling Affect the  
21 Structure of Soda-Lime Glass? *J. Phys. Chem. C* **2010**, *114* (29), 12754–12759.  
22 <https://doi.org/10.1021/jp1033905>.  
23  
24 (16) Redkov, A. V.; Melehin, V. G.; Lipovskii, A. A. How Does Thermal Poling Produce  
25 Interstitial Molecular Oxygen in Silicate Glasses? *J. Phys. Chem. C* **2015**, *119* (30),  
26 17298–17307. <https://doi.org/10.1021/acs.jpcc.5b04513>.  
27  
28 (17) Lopicard, A.; Cardinal, T.; Fargin, E.; Adamietz, F.; Rodriguez, V.; Richardson, K.;  
29 Dussauze, M. Surface Reactivity Control of a Borosilicate Glass Using Thermal  
30 Poling. *J. Phys. Chem. C* **2015**, *119* (40), 22999–23007.  
31 <https://doi.org/10.1021/acs.jpcc.5b07139>.  
32  
33 (18) Lopicard, A.; Cardinal, T.; Fargin, E.; Adamietz, F.; Rodriguez, V.; Richardson, K.;  
34 Dussauze, M. Micro-Structuring the Surface Reactivity of a Borosilicate Glass via  
35 Thermal Poling. *Chem. Phys. Lett.* **2016**, *664*, 10–15.  
36 <https://doi.org/10.1016/j.cplett.2016.09.077>.  
37  
38 (19) Kamenskii, A. N.; Reduto, I. V.; Petrikov, V. D.; Lipovskii, A. A. Effective Diffraction  
39 Gratings via Acidic Etching of Thermally Poled Glass. *Opt. Mater.* **2016**, *62*, 250–  
40 254. <https://doi.org/10.1016/j.optmat.2016.09.074>.  
41  
42 (20) Lind, F.; Palles, D.; Möncke, D.; Kamitsos, E. I.; Wondraczek, L. Modifying the  
43 Surface Wetting Behavior of Soda-Lime Silicate Glass Substrates through Thermal  
44  
45  
46  
47  
48  
49  
50  
51  
52  
53  
54  
55  
56  
57  
58  
59  
60

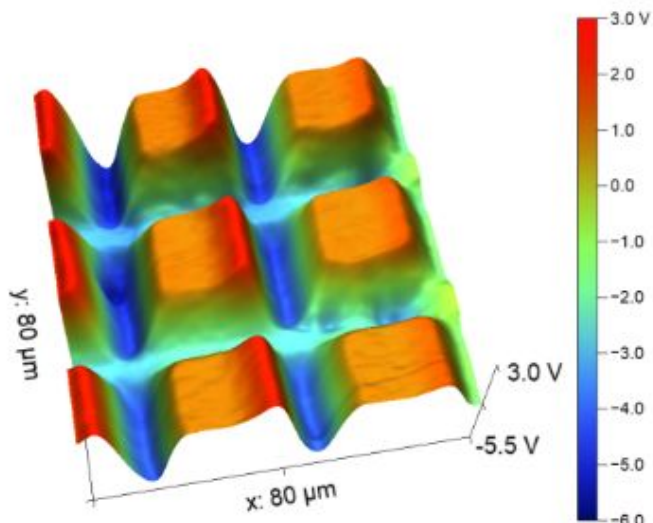
- 1  
2  
3 Poling. *J. Non-Cryst. Solids* **2017**, *462*, 47–50.  
4 <https://doi.org/10.1016/j.jnoncrysol.2017.02.006>.  
5  
6  
7 (21) Yudistira, D.; Faccio, D.; Corbari, C.; Kazansky, P. G.; Benchabane, S.; Pruneri, V.  
8 Electric Surface Potential and Frozen-in Field Direct Measurements in Thermally  
9 Poled Silica. *Appl. Phys. Lett.* **2008**, *92* (1), 012912.  
10 <https://doi.org/10.1063/1.2827175>.  
11  
12  
13 (22) Dussauze, M.; Kamitsos, E. I.; Fargin, E.; Rodriguez, V. Refractive Index  
14 Distribution in the Non-Linear Optical Layer of Thermally Poled Oxide Glasses.  
15 *Chem. Phys. Lett.* **2009**, *470* (1–3), 63–66.  
16 <https://doi.org/10.1016/j.cplett.2009.01.007>.  
17  
18  
19 (23) Myers, R. A.; Mukherjee, N.; Brueck, S. R. Large Second-Order Nonlinearity in  
20 Poled Fused Silica. *Opt. Lett.* **1991**, *16* (22), 1732–1734.  
21  
22  
23 (24) Quiquempois, Y.; Godbout, N.; Lacroix, S. Model of Charge Migration during  
24 Thermal Poling in Silica Glasses: Evidence of a Voltage Threshold for the Onset of  
25 a Second-Order Nonlinearity. *Phys. Rev. A* **2002**, *65* (4).  
26 <https://doi.org/10.1103/PhysRevA.65.043816>.  
27  
28  
29 (25) Dussauze, M.; Cremoux, T.; Adamietz, F.; Rodriguez, V.; Fargin, E.; Yang, G.;  
30 Cardinal, T. Thermal Poling of Optical Glasses: Mechanisms and Second-Order  
31 Optical Properties. *Int. J. Appl. Glass Sci.* **2012**, *3* (4), 309–320.  
32 <https://doi.org/10.1111/ijag.12001>.  
33  
34  
35 (26) Dussauze, M.; Malakho, A.; Fargin, E.; Manaud, J. P.; Rodriguez, V.; Adamietz, F.;  
36 Lazoryak, B. Large Second Order Optical Nonlinearity in Thermally Poled  
37 Amorphous Niobium Borophosphate Films. *J. Appl. Phys.* **2006**, *100* (1), 013108.  
38 <https://doi.org/10.1063/1.2210572>.  
39  
40  
41 (27) Karam, L.; Adamietz, F.; Michau, D.; Gonçalves, C.; Kang, M.; Sharma, R.;  
42 Murugan, G. S.; Cardinal, T.; Fargin, E.; Rodriguez, V.; Richardson, K. A.;  
43 Dussauze, M. Electrically Micro-Polarized Amorphous Sodo-Niobate Film  
44 Competing with Crystalline Lithium Niobate Second-Order Optical Response. *Adv.*  
45 *Opt. Mater.* **2020**, 2000202. <https://doi.org/10.1002/adom.202000202>.  
46  
47  
48  
49  
50  
51  
52  
53  
54  
55  
56  
57  
58  
59  
60

- 1  
2  
3  
4 (28) Deparis, O.; Kazansky, P. G.; Abdolvand, A.; Podlipensky, A.; Seifert, G.; Graener,  
5 H. Poling-Assisted Bleaching of Metal-Doped Nanocomposite Glass. *Appl. Phys.*  
6 *Lett.* **2004**, *85* (6), 872–874. <https://doi.org/10.1063/1.1779966>.  
7  
8  
9 (29) Beresna, M.; Kazansky, P. G.; Deparis, O.; Carvalho, I. C. S.; Takahashi, S.;  
10 Zayats, A. V. Poling-Assisted Fabrication of Plasmonic Nanocomposite Devices in  
11 Glass. *Adv. Mater.* **2010**, *22* (39), 4368–4372.  
12 <https://doi.org/10.1002/adma.201001222>.  
13  
14  
15 (30) Brunkov, P. N.; Melekhin, V. G.; Goncharov, V. V.; Lipovskii, A. A.; Petrov, M. I.  
16 Submicron-Resolved Relief Formation in Poled Glasses and Glass-Metal  
17 Nanocomposites. *Tech. Phys. Lett.* **2008**, *34* (12), 1030–1033.  
18 <https://doi.org/10.1134/S1063785008120122>.  
19  
20  
21 (31) Chervinskii, S.; Sevriuk, V.; Reduto, I.; Lipovskii, A. Formation and 2D-Patterning  
22 of Silver Nanoisland Film Using Thermal Poling and out-Diffusion from Glass. *J.*  
23 *Appl. Phys.* **2013**, *114* (22), 224301. <https://doi.org/10.1063/1.4840996>.  
24  
25  
26 (32) Lopicard, A.; Adamietz, F.; Rodriguez, V.; Richardson, K.; Dussauze, M.  
27 Demonstration of Dimensional Control and Stabilization of Second Harmonic  
28 Electro-Optical Response in Chalcogenide Glasses. *Opt. Mater. Express* **2018**, *8*  
29 (6), 1613. <https://doi.org/10.1364/OME.8.001613>.  
30  
31  
32 (33) Lopicard, A.; Bondu, F.; Kang, M.; Siskin, L.; Yadav, A.; Adamietz, F.; Rodriguez,  
33 V.; Richardson, K.; Dussauze, M. Long-Lived Monolithic Micro-Optics for  
34 Multispectral GRIN Applications. *Sci. Rep.* **2018**, *8* (1), 7388.  
35 <https://doi.org/10.1038/s41598-018-25481-x>.  
36  
37  
38 (34) Griffiths, J. E.; Phillips, J. C.; Espinosa, G. P.; Remeika, J. P.; Bridenbaugh, P. M.  
39 Assignment of the Companion A1c Line in GeX(S, Se)<sub>1-x</sub> Glasses. *Phys. Status*  
40 *Solidi B* **1984**, *122* (1), K11–K15. <https://doi.org/10.1002/pssb.2221220148>.  
41  
42  
43 (35) Bridenbaugh, P. M.; Espinosa, G. P.; Griffiths, J. E.; Phillips, J. C.; Remeika, J. P.  
44 Microscopic Origin of the Companion A 1 Raman Line in Glassy Ge (S, Se)<sub>2</sub>. *Phys.*  
45 *Rev. B* **1979**, *20* (10), 4140–4144. <https://doi.org/10.1103/PhysRevB.20.4140>.  
46  
47  
48 (36) Kawamoto, Y.; Kawashima, C. Infrared and Raman Spectroscopic Studies on  
49 Short-Range Structure of Vitreous GeS<sub>2</sub>. *Mater. Res. Bull.* **1982**, *17* (12), 1511–  
50 1516. [https://doi.org/10.1016/0025-5408\(82\)90206-9](https://doi.org/10.1016/0025-5408(82)90206-9).  
51  
52  
53  
54  
55  
56  
57  
58  
59  
60

- 1  
2  
3  
4 (37) Jackson, K.; Briley, A.; Grossman, S.; Porezag, D. V.; Pederson, M. R. Raman-  
5 Active Modes of a - GeSe<sub>2</sub> and a - GeS<sub>2</sub>: A First-Principles Study. *Phys. Rev. B*  
6 **1999**, *60* (22), R14985–R14989. <https://doi.org/10.1103/PhysRevB.60.R14985>.  
7  
8  
9 (38) Bérubé, J. P.; Messaddeq, S. H.; Bernier, M.; Skripachev, I.; Messaddeq, Y.; Vallée,  
10 R. Tailoring the Refractive Index of Ge-S Based Glass for 3D Embedded  
11 Waveguides Operating in the Mid-IR Region. *Opt. Express* **2014**, *22* (21), 26103.  
12 <https://doi.org/10.1364/OE.22.026103>.  
13  
14  
15 (39) Chazot, M.; Mereau, R.; El Amraoui, M.; Adamietz, F.; Messaddeq, Y.; Rodriguez,  
16 V. Multimodal Structural Characterization of Ge–S–I Glasses by Combination of  
17 DFT Calculation and IR and Polarized Raman Spectroscopy. *J. Phys. Chem. C*  
18 **2019**, *123* (6), 3758–3769. <https://doi.org/10.1021/acs.jpcc.8b11187>.  
19  
20  
21 (40) Masselin, P.; Le Coq, D.; Cuisset, A.; Bychkov, E. Spatially Resolved Raman  
22 Analysis of Laser Induced Refractive Index Variation in Chalcogenide Glass. *Opt.*  
23 *Mater. Express* **2012**, *2* (12), 1768. <https://doi.org/10.1364/OME.2.001768>.  
24  
25  
26 (41) Koudelka, L.; Frumar, M.; Pisárčik, M. Raman Spectra of Ge-Sb-S System Glasses  
27 in the S-Rich Region. *J. Non-Cryst. Solids* **1980**, *41* (2), 171–178.  
28 [https://doi.org/10.1016/0022-3093\(80\)90162-3](https://doi.org/10.1016/0022-3093(80)90162-3).  
29  
30  
31 (42) Susarla, S.; Tsafack, T.; Owuor, P. S.; Puthirath, A. B.; Hachtel, J. A.; Babu, G.;  
32 Apte, A.; Jawdat, B. I.; Hilario, M. S.; Lerma, A.; et al. High-K Dielectric Sulfur-  
33 Selenium Alloys. *Sci. Adv.* **2019**, *5* (5), eaau9785.  
34 <https://doi.org/10.1126/sciadv.aau9785>.  
35  
36  
37 (43) Ward, A. T. Raman Spectroscopy of Sulfur, Sulfur-Selenium, and Sulfur-Arsenic  
38 Mixtures. *J. Phys. Chem.* **1968**, *72* (12), 4133–4139.  
39 <https://doi.org/10.1021/j100858a031>.  
40  
41  
42 (44) Pfister, G. Electronic Properties of Chalcogenide Glasses and Their Use in  
43 Xerography. *J. Electron. Mater.* **1979**, *8* (6), 789–837.  
44 <https://doi.org/10.1007/BF02651186>.  
45  
46  
47 (45) Mikla, V. I.; Mikla, V. V. Xerographic Spectroscopy of Gap States in Se-Rich  
48 Amorphous Semiconductors Review. *J. Non-Cryst. Solids* **2011**, *357* (22–23),  
49 3675–3688. <https://doi.org/10.1016/j.jnoncrysol.2011.07.018>.  
50  
51  
52  
53  
54  
55  
56  
57  
58  
59  
60

- 1  
2  
3  
4 (46) Pfister, G.; Scher, H. Dispersive (Non-Gaussian) Transient Transport in Disordered  
5 Solids. *Adv. Phys.* **1978**, *27* (5), 747–798.  
6 <https://doi.org/10.1080/00018737800101474>.  
7  
8  
9 (47) Yuan, N.; Li, J. SiO<sub>2</sub> Film Electret with High Surface Potential Stability. *Appl. Surf.*  
10 *Sci.* **2005**, *252* (2), 455–460. <https://doi.org/10.1016/j.apsusc.2005.01.025>.  
11  
12 (48) Andriesh, A. M.; Buzdugan, A. I.; Zelenina, L. I.; Shutov, S. D. Dark Decay of  
13 Surface Potential in Vitreous As<sub>2</sub>S<sub>3</sub>. *Phys. Status Solidi A* **1982**, *74* (1), K79–K82.  
14 <https://doi.org/10.1002/pssa.2210740161>.  
15  
16 (49) Schnörer, H.; Haarer, D.; Blumen, A. Crossover from Dispersive to Nondispersive  
17 Transport in a Trap-Controlled Hopping Model. *Phys. Rev. B* **1988**, *38* (12), 8097–  
18 8101. <https://doi.org/10.1103/PhysRevB.38.8097>.  
19  
20 (50) Godzik, K.; Schirmacher, W. Theory of dispersive transport in amorphous  
21 semiconductors. *J. Phys. Colloq.* **1981**, *42* (C4), C4-127-C4-131.  
22 <https://doi.org/10.1051/jphyscol:1981424>.  
23  
24 (51) Phillips, J. C. Stretched Exponential Relaxation in Molecular and Electronic  
25 Glasses. *Rep. Prog. Phys.* **1996**, *59* (9), 1133–1207. [https://doi.org/10.1088/0034-](https://doi.org/10.1088/0034-4885/59/9/003)  
26 [4885/59/9/003](https://doi.org/10.1088/0034-4885/59/9/003).  
27  
28 (52) Shimakawa, K.; Inami, S.; Elliott, S. R. Reversible Photoinduced Change of  
29 Photoconductivity in Amorphous Chalcogenide Films. *Phys. Rev. B* **1990**, *42* (18),  
30 11857–11861. <https://doi.org/10.1103/PhysRevB.42.11857>.  
31  
32 (53) Shoulders, W. T.; Novak, J.; Dussauze, M.; Musgraves, J. D.; Richardson, K.  
33 Thermal Poling Behavior and SHG Stability in Arsenic-Germanium Sulfide Glasses.  
34 *Opt. Mater. Express* **2013**, *3* (6), 700. <https://doi.org/10.1364/OME.3.000700>.  
35  
36 (54) Redkov, A. V.; Melehin, V. G.; Statcenko, V. V.; Lipovskii, A. A. Nanoprofiling of  
37 Alkali-Silicate Glasses by Thermal Poling. *J. Non-Cryst. Solids* **2015**, *409*, 166–169.  
38 <https://doi.org/10.1016/j.jnoncrysol.2014.11.007>.  
39  
40  
41  
42  
43  
44  
45  
46  
47  
48  
49  
50  
51

52 **TOC graphic**  
53  
54  
55  
56  
57  
58  
59  
60



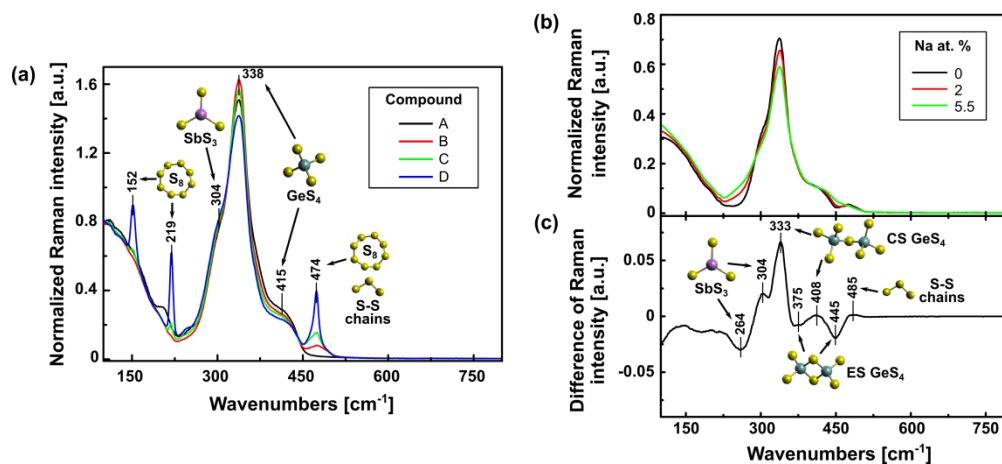


Figure 1. Raman spectra of the pristine ChG samples: (a) A, B, C and D glasses series with increasing S/Ge ratio, (b) Na0, Na2 and Na5.5 glasses series with increasing sodium content and constant ratio between the other components and (c) Raman difference spectra: response of Na5.5 subtracted to Na0 response.

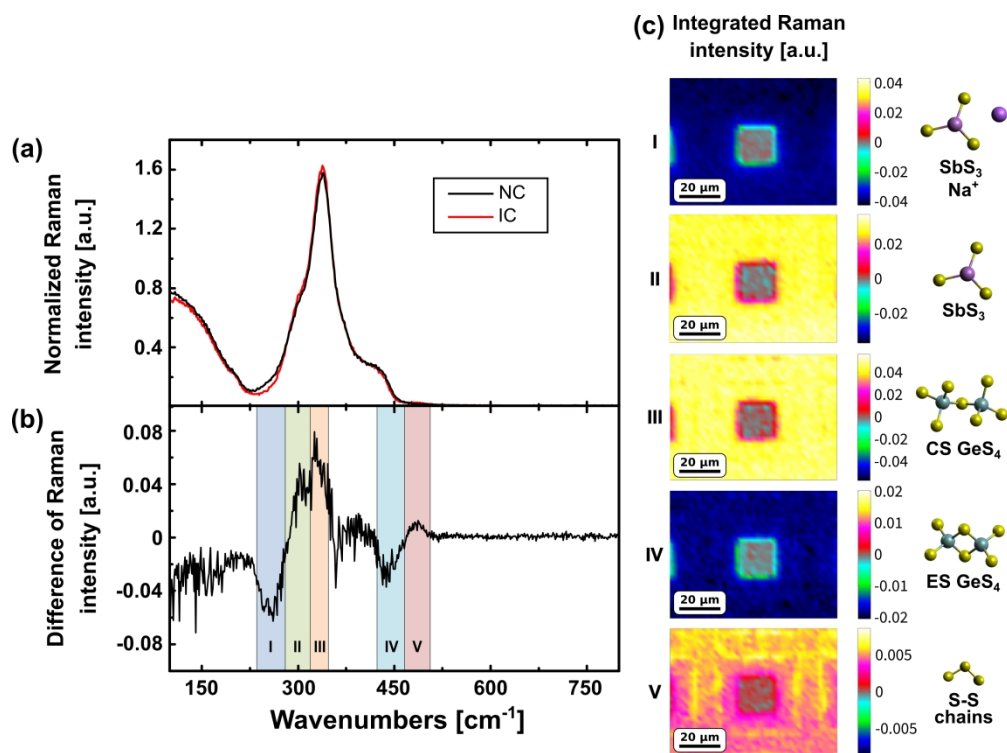


Figure 2. (a) Raman spectra from the thermally poled A glass, the black line corresponds to the region non in contact (NC) with the conductive zone and the red line in contact (IC). (b) Raman difference spectrum where the spectrum of the NC region has been subtracted to the IC region. (c) Spatial evolution of the Raman intensity of the different bands revealed by the Raman difference spectrum and the schematic representation of the glass units they are associated with.

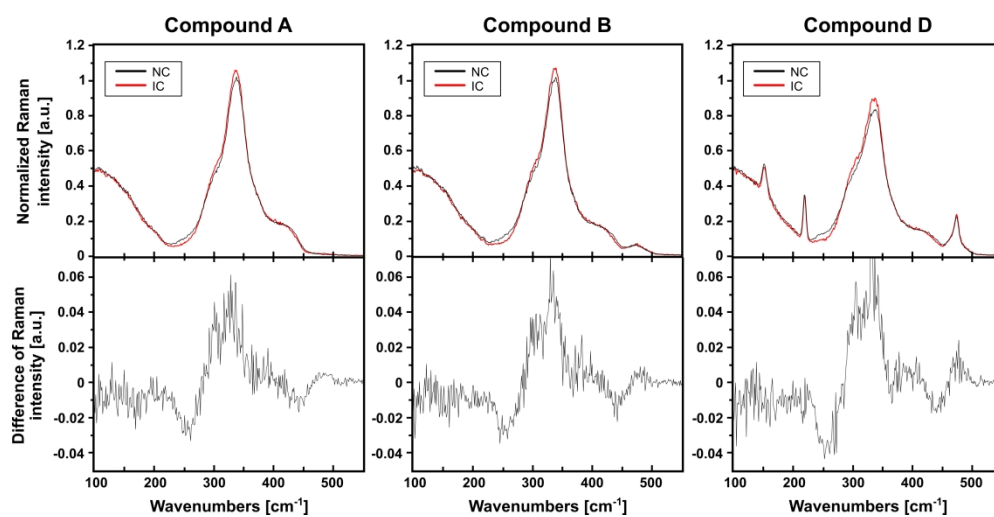


Figure 3. (Top) Raman spectra from the different thermally poled glasses A, B and D presenting different S/Ge ratio and same sodium content. The black lines correspond to the region not in contact (NC) with the conductive zone and the red line in contact (IC). (Bottom) Raman different spectra for each glass where the spectrum of the NC region has been subtracted from the spectrum of the IC region.

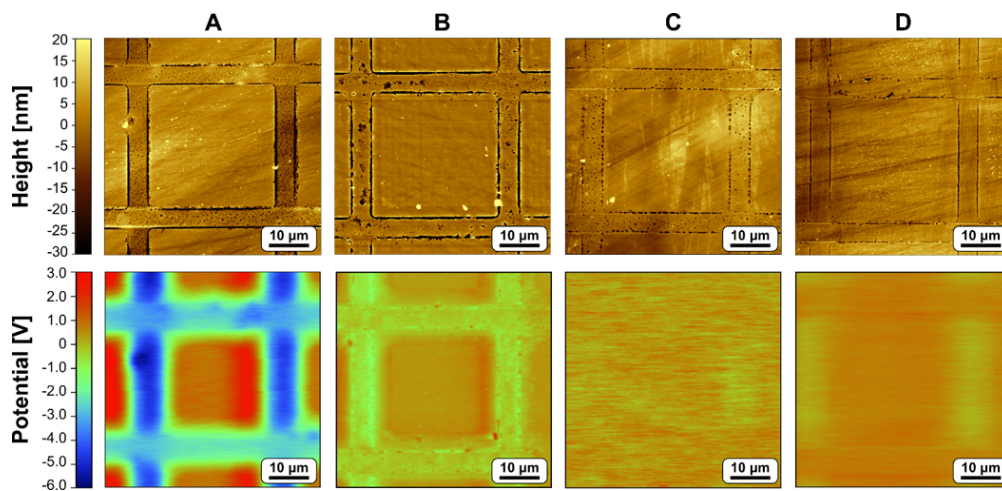


Figure 4. AFM measured topography (top) and KPFM measured surface potential (bottom) images of the post-poling surface of glasses A, B, C and D i.e. increasing sulfur content with fixed sodium content.

178x84mm (150 x 150 DPI)

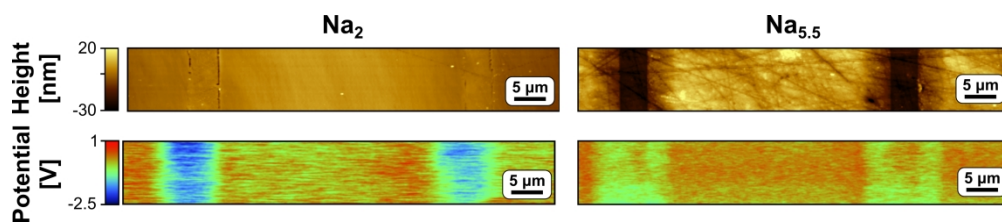


Figure 5. AFM measured topography (top) and KPFM measured surface potential (bottom) images of the post-poling surface of glasses  $\text{Na}_2$  and  $\text{Na}_{5.5}$  i.e. increasing sodium content with other component's ratios constant. The results obtained for  $\text{Na}_0$  (no sodium) are not presented as no effect – topology or potential – were observed in the absence of alkali cation in the initial composition.

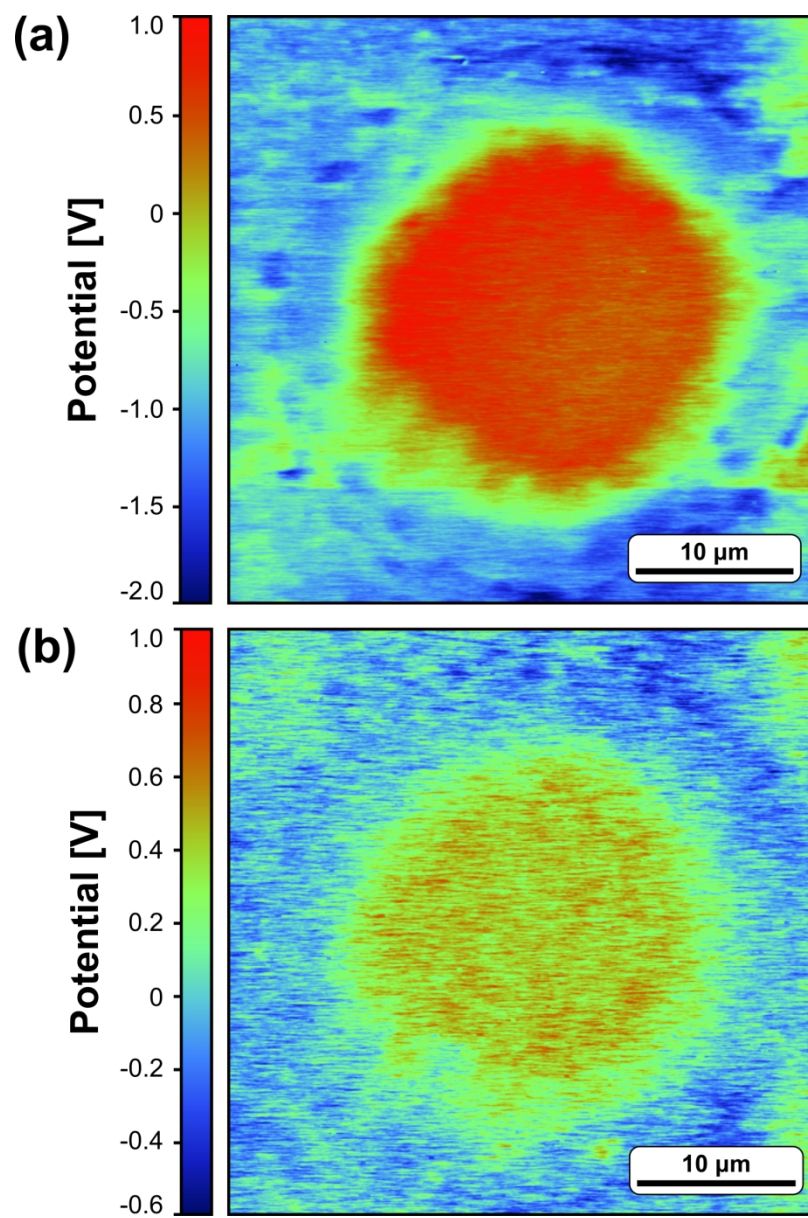


Figure 6. KPFM imaging of a thermally poled glass B using a disk pattern on the electrode measured just after the treatment (a) and after 24 months (b).